Charge conduction and relaxation in $Ca_{1-x}Dy_xBaFe_4O_7$

M. Islam,[1] S. K. Adhikari,[2] S. Adhikari,[1] S. Chatterjee,[2] S. Goswami,[3] D. De,[3,4] K. A. Irshad,[5] B. Joseph,[5] W. Caliebe,[6] and A. Karmakar[1,*]

[1] *Department of Physics, Surya Sen Mahavidyalaya, Siliguri 734 004, India*
[2] *UGC-DAE Consortium for Scientific Research, Kolkata Centre, Sector III, LB-8, Salt Lake, Kolkata 700 106, India*
[3] *Material Science Research Lab, The Neotia University, Sarisa, D.H. Road, 24 Pgs (South), West Bengal, 743 368, India*
[4] *Department of Physics, Sukumar Sengupta Mahavidyalaya, State Highway 7, Keshpur, Paschim Medinipur, 721 150, West Bengal, India*
[5] *Elettra Sincrotrone Trieste S.C.p.A., SS 14-km 163.5, 34149 Basovizza, Italy*
[6] *Deutsches Elektronen-Synchrotron DESY, Notkestrasse 85, D-22607 Hamburg, Germany*

The article presents in-depth studies of the dielectric properties and conduction dynamics of Dy doped $CaBaFe_4O_7$ which is a recently characterized magnetoelectric material with strong potentials for technological applications as it shows a near room temperature ferrimagnetic transition along with strong ferrimagnetic moment, and gigantic electric polarization change. This work demonstrates the direct correlation of the dielectric, and electrical transport properties of $Ca_{1-x}Dy_xBaFe_4O_7$ (x = 0, 0.01, 0.03, and 0.05) with structural distortion through various dc, ac conduction, high-energy x-ray diffraction studies, and modeling of the data. $CaBaFe_4O_7$ has a unique structure characterized by alternate stacking of FeO_4 tetrahedra in triangular and kagomé layers. Large structural distortion, competing magnetic interactions, exchange striction effects and possible charge ordering are expected to play a major role in the dielectric and electrical properties of the material. We report observation of short-range polaron hopping conduction mechanism in the low-temperature regime and signature of large polaronic nature of charge carriers. Modeling of the electric modulus using Havriliak-Negami equation points out both distribution and cooperativeness in the polaron dynamics, which can be correlated to the interplay of structural distortion and the background electric field due to the polar nature of the materials. The Havriliak-Negami parameters closely follow orthorhombic distortion of the structures.

I. INTRODUCTION

The *Swedenborgites* $CaBaM_4O_7$ (M is generally Co or Fe) are a relatively new class of magnetoelectric materials which show very strong electric polarization coupled to quite robust long-range ferrimagnetic order [1–3]. These are distinctive members in the transition metal oxides family harboring competing magnetic interactions as these exhibit unique 2D layering of alternate triangular and kagomé patterns of interconnected MO_4 tetrahedra. $CaBaFe_4O_7$, among these, is particularly quite attractive as it shows a near-room temperature ferrimagnetic transition. Single crystal studies demonstrated a Curie temperature $T_C \sim 290$ K from inverse magnetic susceptibility [2], and ~ 275 K from specific heat capacity [3]. While till date the most archetypal and widely studied room temperature multiferroic material is $BiFeO_3$ [4], $CaBaFe_4O_7$ can be a very fascinating magnetoelectric material with useful functional properties, if its transition temperature can be tuned towards room temperature, owing to its attractive electric polarization and ferrimagnetic moment [2, 3]. The geometrical frustration, such as in its sister compounds - $YbBaCo_4O_7$, $YBaFe_4O_7$, etc. [5–8], is lifted due to strong distortion in $CaBaFe_4O_7$, so that now the structure is more asymmetric. This consequently leads to long range magnetic ordering with a magnetization of ~ 5 μ_B/f.u. at 0.5 T field along the c-direction, and ~ 5 μ_B/f.u. at 14 T field perpendicular to the c-direction at 80 K, a gigantic field induced electric polarization change with a maximum value of $\Delta P = 850$ μC/m^2 at 80 K with a large linear magnetoelectric coupling $\alpha_{cc} \approx 39$ ps/m along the c-direction [3]. Tuning this structural distortion can thus be a means to control T_c, while it can further be controlled by directly modifying the magnetic interactions between Fe ions by doping other suitable transition metals in Fe sites. For example, doping of K at the Ba-site, or Pr or Nd at the Ca-site, with up to 20% doping, induced spin-glass or cluster-glass states, with the appearance of additional freezing transitions (T_f = 115 or 110 K) for the Pr/Nd doped compounds, due to the reduction of orthorhombic distortion and strengthening of geometrical frustration [9]. Doping of non-magnetic La for Ca ($\leq 5\%$) led to a linear increase of T_c from 62.5 to 66.5 K, and enhancement of electric polarization, because of a considerable increase of structural distortion below 87 K [10].

The pyroelectric materials $CaBaM_4O_7$ are polar along the c-direction with non-switchable polarization, both in the paramagnetic and ferrimagnetic phases, as studied in the case of $CaBaCo_4O_7$ [11]. Notably, $CaBaFe_4O_7$, along with $CaBaCo_4O_7$, are the only members among its sister compounds that possess the long range (ferri)magnetic ordering [3]. Besides, the electric polarization and the ferrimagnetism were found interrelated via exchange-

* akarmakar@suryasencollege.org.in

striction effects [2, 3, 12]. This designates the materials as spin-induced magnetoelectrics. $CaBaFe_4O_7$ shows a strong ferrimagnetic magnetization due to a modest magnetic field of $\sim$ 1 T or lesser and large change in polarization (ΔP) but at high magnetic fields $\sim$ 10 T or larger [3, 13]. Moreover, $CaBaFe_4O_7$ might have a strong pyroelectric polarization change at the T_C close to room temperature, similar to $CaBaCo_4O_7$, mediated via magnetostriction [14]. The considerable conductivity of the material however poses a hindrance for its measurement and applicability [3]. Nevertheless, doping studies in the material may prove to be fruitful for increasing both the low field ΔP and the resistivity for viable applications. For example, Ni doping not only led to a drastic four-fold increase of pyroelectric polarization in $CaBaCo_{3.96}Ni_{0.04}O_7$ but also radically improved the field induced change in pyroelectric polarization by about six times, compared to $CaBaCo_{3.96}Cr_{0.04}O_7$ [15], while simultaneously increasing the resistivity by about three orders of magnitude [16]. The potential applications of the material may include low temperature pyroelectric sensors or thermometers, infrared sensing devices, solar energy pyroelectric converters, passive infrared sensors, and not to miss possible electrocaloric and magnetocaloric applications [11, 12, 17]. Another interesting effect in the material would be a large change in polarization in the single crystal ($\sim$ 300 $\mu C/m^2$ or larger) if a magnetic field ($\sim$ 5 T or larger) is rotated about an axis perpendicular to the c-axis [3], which may find applications. However, exploiting the rich attributes of the materials requires a profound knowledge of the dielectric properties. This article is devoted to the study of dielectric properties along with dc and ac conduction dynamics of $CaBaFe_4O_7$ and three electron doped derivatives, namely, $Ca_{0.99}Dy_{0.01}BaFe_4O_7$, $Ca_{0.97}Dy_{0.03}BaFe_4O_7$, and $Ca_{0.95}Dy_{0.05}BaFe_4O_7$. We have selected $CaBaFe_4O_7$ because of its near-room temperature T_c and have used very low doping percentage of Dy ($\leq$ 5%) at the Ca-site with a motive to tune the structural distortion and study its effects on the dielectric properties and conduction dynamics. Dy is a trivalent rare-earth element having a slightly smaller ionic radius than the divalent Ca and has one of the largest magnetic moments among the rare-earths. We will see in the following that the properties are directly related to the structural distortion. Hopefully, the information obtained from this study will aid in the process of technological applications of these materials.

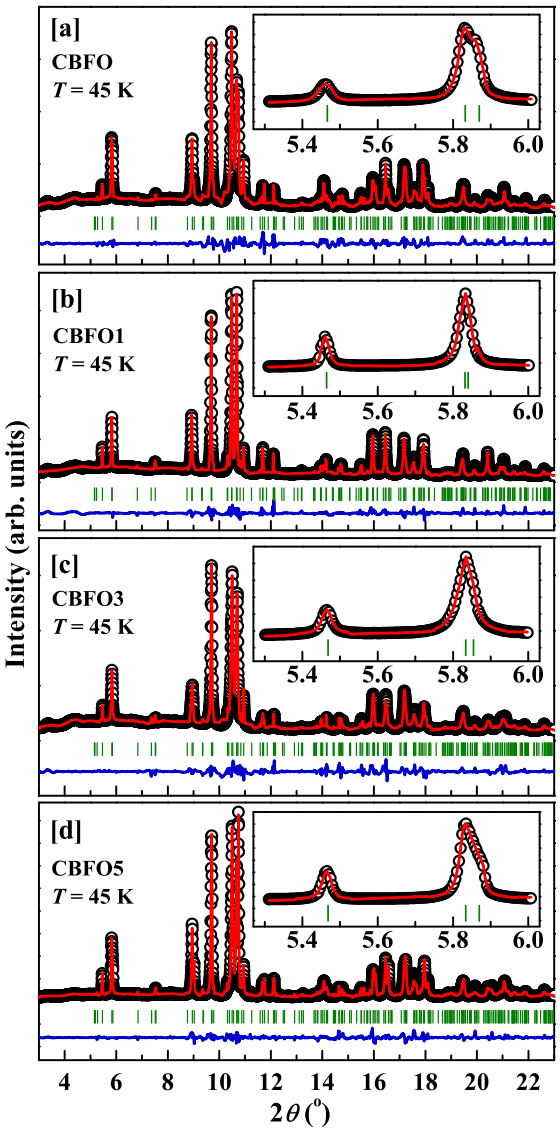

FIG. 1. Powder x-ray diffraction plots at 45 K with $\lambda = 0.4957$ Å , and Rietveld refinement fits of (a) CBFO, (b) CBFO1, (c) CBFO3, and (d) CBFO5. The black symbols represent the experimental data points and the red solid curves represent the calculated diffraction patterns. The blue curves are the difference plots and the green markers are the positions of Bragg reflections. The inset in each figure displays an enlarged view of the two peaks in between $2\theta = 5.3°$, and 6°.

II. EXPERIMENTAL TECHNIQUES

Polycrystalline samples of $CaBaFe_4O_7$ (CBFO), $Ca_{0.99}Dy_{0.01}BaFe_4O_7$ (CBFO1), $Ca_{0.97}Dy_{0.03}BaFe_4O_7$ (CBFO3), and $Ca_{0.95}Dy_{0.05}BaFe_4O_7$ (CBFO5) were prepared using solid state reaction technique. $CaCO_3$, $BaCO_3$, Dy_2O_3, FeO, and Fe_2O_3 with the purity of at least 99.99% were used as the starting chemicals. Stoichiometric masses of the chemicals were initially mixed and calcined at 900 °C. The mixture was then thoroughly ground and pressed into pellets and heated at 1100 °C for 12 h. This step was repeated once more for homogeneity. The samples were then reduced in a flowing 5% H_2-Ar gas mixture at 1000 °C for 12 h twice, first in powder form and then in pellet form, and then slow cooled to room temperature.

The samples were tested for single phase crystallization in the laboratory by x-ray powder diffraction experiments using a Bruker D8-Advance X-ray powder diffractome-

TABLE I. Structural parameters of CBFO, CBFO1, CBFO3, and CBFO5 at 45 K, analyzed using the orthorhombic $Pbn2_1$ space group.

	CBFO			**CBFO1**			**CBFO3**			**CBFO5**		
						Lattice parameters						
	a (Å)	b (Å)	c (Å)	a (Å)	b (Å)	c (Å)	a (Å)	b (Å)	c (Å)	a (Å)	b (Å)	c (Å)
	6.2998(4)	11.0308(1)	10.3871(1)	6.3546(1)	11.0357(1)	10.3986(7)	6.3413(6)	11.0397(4)	10.3992(7)	6.2986(9)	11.0259(1)	10.3857(9)
						Fractional atomic positions						
Atoms	x	y	z	x	y	z	x	y	z	x	y	z
Ca/Dy	-0.0568(3)	0.6761(7)	0.8680(1)	-0.0088(4)	0.6654(0)	0.8701(2)	-0.0097(7)	0.6837(5)	0.8646(9)	-0.0414(0)	0.6736(3)	0.8609(4)
Ba	-0.0074(3)	0.6649(9)	0.5000	-0.0358(5)	0.6661(0)	0.5000	-0.0143(3)	0.6735(1)	0.5000	-0.0073(5)	0.6653(5)	0.5000
Fe1	0.0056(7)	0.0004(8)	0.9297(1)	0.0042(9)	0.0081(6)	0.9369(7)	0.0070(8)	0.0003(7)	0.9405(0)	0.0050(9)	0.0005(0)	0.9381(4)
Fe2	0.0000	0.1824(6)	0.6815(7)	0.0000	0.1715(4)	0.6804(7)	0.0000	0.1812(0)	0.6917(0)	0.0000	0.1805(8)	0.6948(1)
Fe3	0.2856(9)	0.0994(3)	0.1779(7)	0.2858(1)	0.0874(2)	0.1747(9)	0.2800(1)	0.0852(8)	0.1792(7)	0.2833(3)	0.0839(5)	0.1821(0)
Fe4	0.2465(3)	0.9166(0)	0.6833(1)	0.2536(0)	0.9217(1)	0.6871(4)	0.2526(8)	0.9151(5)	0.6792(5)	0.2550(3)	0.9134(4)	0.6936(6)
O1	0.0191(8)	0.0034(1)	0.2478(7)	0.0182(7)	0.0026(1)	0.2531(5)	0.0176(7)	0.0013(6)	0.2577(1)	0.0188(7)	0.0015(7)	0.2550(3)
O2	0.0000	0.5060(1)	0.2328(8)	0.0000	0.4893(0)	0.2353(9)	0.0000	0.5013(0)	0.2326(1)	0.0000	0.5029(5)	0.2358(7)
O3	0.7762(8)	0.2595(5)	0.7858(1)	0.7819(4)	0.2615(3)	0.7814(3)	0.7760(6)	0.2584(8)	0.7843(7)	0.7723(8)	0.2635(1)	0.7817(3)
O4	0.7370(9)	0.7499(5)	0.2249(8)	0.7324(8)	0.7532(2)	0.2302(9)	0.7341(7)	0.7534(2)	0.2269(9)	0.7311(3)	0.7516(2)	0.2210(3)
O5	-0.0480(4)	0.1484(9)	0.5046(0)	-0.0432(3)	0.1589(0)	0.5134(7)	-0.0492(2)	0.1527(9)	0.5027(1)	-0.0497(0)	0.1530(0)	0.5012(9)
O6	0.2047(0)	0.1102(4)	0.0093(8)	0.2044(4)	0.1109(2)	0.0056(6)	0.1980(8)	0.0951(6)	0.0069(2)	0.2073(9)	0.1003(7)	0.0072(2)
O7	0.2561(1)	0.9480(6)	0.5000	0.2619(0)	0.9556(4)	0.5000	0.2548(8)	0.9468(3)	0.5000	0.2523(3)	0.9506(5)	0.5000

ter with Cu-K_α radiation (λ = 1.5406 Å). Final x-ray powder diffraction experiments were performed in Xpress beamline of Elettra Sincrotrone Trieste with monochromatic x-rays of wavelength 0.4957 Å. Data were collected at seven different temperatures − 23, 45, 100, 150, 205, 255, and 295 K, using a DECTRIS PILATUS 3S 6M 2D detector. Low temperature was achieved using a CCR. Rietveld refinement of the data was done using `FullProf` suite [18] and visualization of the crystal structure was done using `VESTA` software [19]. XAFS measurements at Fe K-edge were performed in the transmission mode in `Advanced XAFS (P64)` beamline in PETRA III light source of DESY equipped with an energy range of 4−44 keV, generated by Si(111) and Si(311) double crystal monochromator [20]. In this article we refer only to the XANES part to ascertain the correct valence states of Fe in the samples. The dc resistivity and ac dielectric data were recorded using a commercial He CCR (Cryo Industries of America), wired internally and externally using coaxial cables, connected with a Keysight E4980A precision LCR meter and Keithley 2450 source meter. Standard four probe technique was used for both dc and ac measurements. For electrical connections with the samples, electrodes were fabricated using air drying conducting silver paste, dried over 2 h in 200 °C in a vacuum environment. Dc resistance was measured in the constant current mode using a 2450 source meter with a current of 5 μA, without any bias voltage. For dielectric measurements, disc shaped parallel plate capacitors were fabricated with $\sim$ 0.4 mm thick discs of samples as the dielectric medium and conducting silver paste on either side as electrode. Care was taken that the electrodes fabricated remain well inside the edges of the samples to minimize edge effects. Capacitance (C), and conductance (G) were measured as the direct quantities and real dielectric permittivity (ϵ'), real total ac conductivity ($\sigma_{\rm tot}$) and electric modulus (M' and M'') were calculated from these two using standard formulas. Amplitude of the ac signal used was 1 V and bias voltage was kept zero. Before measurements with the sample, 'open' and 'short' correction measurements were performed in the meter connected with the wiring up to the sample in order to eliminate the wiring and ambient capacitance and conductance. The frequency (f) range available was 20 Hz − 2 MHz.

III. RESULTS AND DISCUSSIONS

A. Structural Analysis and Morphology

Representative plots of x-ray powder diffraction at 45 K are shown in Fig. 1 for all the samples, along with the respective Rietveld refinement fits. The data are fitted with orthorhombic $Pbn2_1$ space group. The fits are quite satisfactory, as obvious from the blue difference plots as well as from the acceptable values of various refinement parameters. The inset of each figure displays an enlarged view of the two peaks in between 2θ = 5.3°, and 6° in order to highlight the data and the fit qualities. The fitting parameters are shown in Table I. The parameters obtained are similar to a previous analysis, with some exceptions [2]. Rietveld refinement plots of the diffraction data at all other temperatures for all the samples, and the refinement parameters are included in the supplemental material file [21]. The curious structure of the materials exhibits alternate stacking of two dimensional layers of triangular and kagomé patterns of Fe ions, encased in corner sharing FeO_4 tetrahedra. The triangular layer consists of the Fe1 sites whereas the kagomé layer houses the Fe2 , Fe3, and Fe4 sites. The two layers of CBFO1 (as an example) is displayed in Fig. 2, as per the actual structure at 45 K. The red tetrahedra (Fe1) occupy

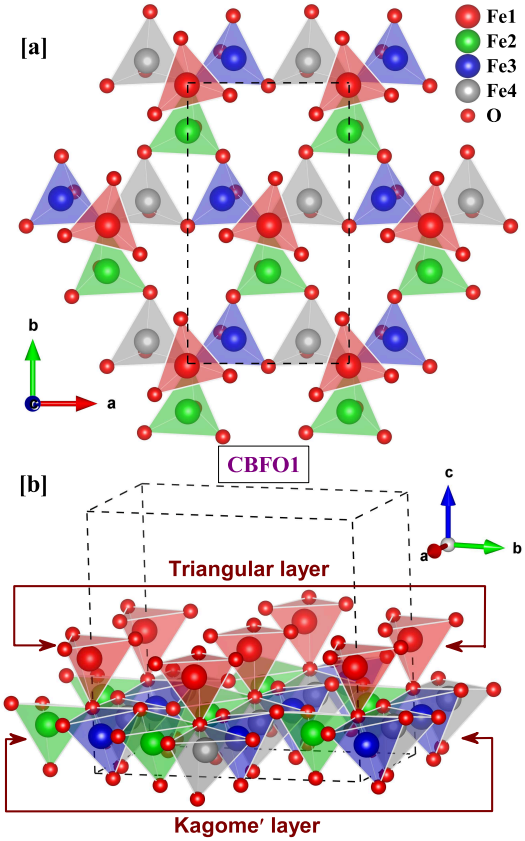

FIG. 2. Crystal structure of CBFO1 at 45 K as a representative sample, exhibiting the four Fe tetrahedra (Fe1, Fe2, Fe3, and Fe4). (a) shows two consecutive layers − triangular and kagomé lattices, viewed along the $-c$ direction. (b) shows the same two layers in a perspective view. The red tetrahedra corresponds to Fe1 in the triangular layer while the green, blue and gray tetrahedra correspond to Fe2, Fe3, and Fe4, respectively, in the kagomé layer. The dashed lines constitute the unit cell. Only two layers are shown for clarity. In the actual structure, two more such layers may be assumed to be repeated in Fig. (b) along the c direction to fill the unit cell along c.

the triangular layer while the green (Fe2), blue (Fe3) and gray (Fe4) tetrahedra represent the kagomé layer. The structure, as viewed along the c-axis, is shown in Fig. 2(a) and a perspective view is shown in Fig. 2(b). The orthorhombic unit cell is illustrated by the dashed lines. For clarity, only one triangular layer and one kagomé layer is shown in the lower half of the unit cell. The upper half contains one more of each of the layers. Strong buckling, tilting and rotation of the tetrahedra leading to orthorhombic distortion of the structure are evident in the pictures. The aspects of distortion is reviewed in details in section III F. The bulk nature of the samples is apparent from the SEM images displayed in Fig. 3(a), (b), (c), and (d). The images confirm that the major volume fraction of the samples have particle sizes higher than 10 μm. Consequently, it is expected that the grain-intrinsic response would be significant in the transport

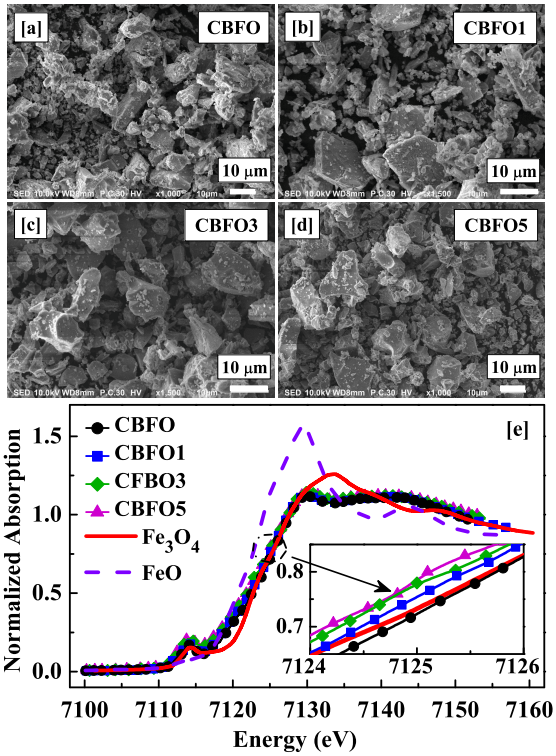

FIG. 3. (a), (b), (c), and (d): SEM images of CBFO, CBFO1, CBFO3, and CBFO5, respectively. (e): Transmission mode Fe K-edge XANES spectrum at 300 K of CBFO, CBFO1, CBFO3, and CBFO5, respectively, along with two standard samples, FeO, and Fe_3O_4. The inset enlarges a portion of the edge to highlight the fine shifts of the curves due to Dy doping.

properties.

B. XANES Spectra

In order to verify the oxidation states of Fe in the samples we have used XANES spectra obtained from XAFS measurements performed in the transmission mode at the Fe K-edge. The XANES part of the spectra of CBFO, CBFO1, CBFO3, and CBFO5 at 300 K are shown in Fig. 3(e) along with FeO (having Fe in 2+ state) and Fe_3O_4 (having Fe in an average 2.5+ state). It is clear that the absorption edges of all the samples match well with the edge of Fe_3O_4, indicating that the average valence states are close to 2.5+, as reported earlier for CBFO [22]. Accordingly, the oxygen stoichiometry of the samples must be close to O_7 for all the samples. It may however be noted that the doping of Dy at the Ca site changes the valence state of Fe by a subtle amount from 2.5+, as in CBFO. The maximum doping percent of Dy, 5% in CBFO5, results in 0.0125 ($\approx$ 0.5%) change in average valence of Fe resulting in a calculated value of 2.4875 while the others result in 2.4975 (0.1% change in CBFO1), and 2.4925 (0.3% change in CBFO3). The

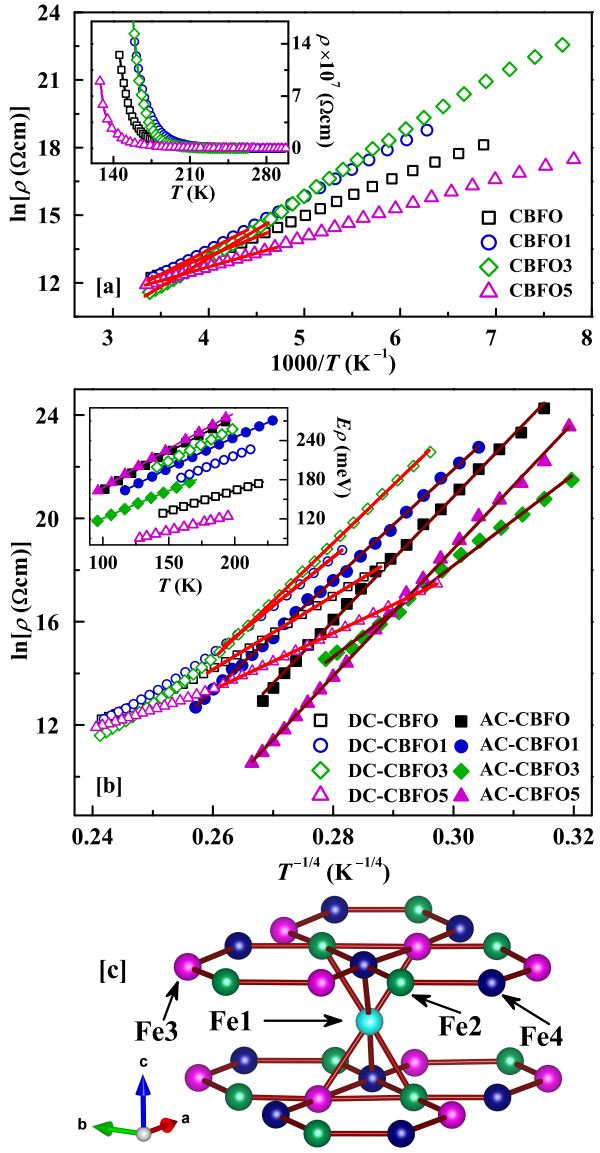

FIG. 4. (a) Temperature dependence of dc resistivity [$\rho(T)$] plotted according to the Arrhenius model, Eq. 1, for all the compounds. The inset represents the semiconducting nature of the variation of ρ with T. (b) $\rho(T)$ plotted according to the VRH model, Eq. 2, for all the compounds. The open symbols represent the data obtained from dc resistivity measurements while the filled symbols represent the data obtained from ac conductivity analysis using Eq. 5. The red and wine solid lines in (a), and (b) are the fits according to the respective models. Inset of (b) represents the range of activation energy in the VRH model, for all the samples, calculated using Eq. 3. (c) Structure of CBFO3 at 300 K, plotted to demonstrate the nearest-neighbor Fe−Fe distances.

XANES spectra indeed exhibits systematic but minute shifts for such changes. This is highlighted in the inset of Fig. 3(e). The red solid curve in the inset represents Fe_3O_4 which is closer to the curve of CBFO, while the curves for the other samples gradually shift towards lower energy.

C. DC resistivity analysis

Dc resistivity data with temperature (T) is shown in Fig. 4(a), and (b), plotted according to two different models. In general, semiconducting nature of dc resistivity was observed in the entire range below 300 K, shown in the inset of Fig. 4(a). A narrow high-T range, above $\sim$ 220 K, could be explained according to the Arrhenius model, as shown in Fig. 4(a). Arrhenius model is defined by the equation

$$\rho = \rho_0 \exp(E_a/k_B T) \tag{1}$$

where ρ_0 is a pre-exponential factor, E_a is the activation energy and k_B is the Boltzmann constant. The fitting indicates that the conduction in the high-T range is dominated by long-range percolation of charge carriers by hopping over potential barriers when the thermal energy is high. Basically the charge carriers are activated beyond the mobility edge. The respective activation energies are listed in Table II.

Resistivity below $\sim$ 220 K has a different behavior. Data in this regime is explained by Variable Range Hopping (VRH) model for all the samples [23]. Fitting with this model suggests that in this T-regime, where the thermal energy is low compared to the disorder energy (such as that arising from crystal defects), the charge carriers perform phonon assisted quantum tunneling to favorable localized sites, not necessarily nearest neighbors, which is commonly called polaron hopping conduction. This hopping occurs in the vicinity of Fermi energy. The mathematical behavior of resistivity (ρ) in this model is described as

$$\rho = \rho_0 \exp(T_0/T)^{1/4} \tag{2}$$

where ρ_0, and T_0 are constants [24]. Fitting using this equation is shown in Fig. 4(b) (open symbols) from which an estimate of T_0 is obtained. Activation energy (E_ρ) can then be calculated as

$$E_\rho = 0.25 k_B T_0^{1/4} T^{3/4}. \tag{3}$$

The activation energy in this model varies with temperature and the range of values obtained for our samples are plotted in the inset of Fig. 4(b) using open symbols. Values obtained from the VRH analysis are listed in Table II. The order of activation energies obtained from the

TABLE II. Parameters obtained from dc resistivity analysis according to Arrhenius, and VRH models.

Sample	Arrhenius model		VRH model				
	E_a (meV)	T-range (K)	$T_0^{1/4}$ ($K^{1/4}$)	E_ρ (meV)	ξ (Å)	R (Å)	T-Range (K)
CBFO	143(±0.3)	216−300	142.49(±0.1)	128−175	3.17	35−32	145−220
CBFO1	188(±0.4)	227−300	189.42(±0.1)	183−228	3.19	46−43	159−213
CBFO3	217(±0.5)	216−300	225.91(±0.1)	198−259	3.18	56−51	140−200
CBFO5	105(±0.1)	190−300	110.08(±0.1)	90−125	3.18	28−25	127−197

fits agrees well with other materials exhibiting polaron hopping conduction, such as FeTiMO_6 (M = Ta, Nb, Sb) [25], Bi-substituted Co_2MnO_4 [26], manganites [27–30], etc. An estimate of the range of hopping (R) is calculated using the equation

$$R \approx 0.2686\,\xi \left(\frac{T_0}{T}\right)^{1/4}, \tag{4}$$

where ξ is the decay length of the polaron wave function. Electron injection in oxides commonly occurs by the generation of random oxygen vacancies which eventually ionize to introduce electrons [31–34]. Moreover, our materials are characterized by regularly arranged Fe^{2+}, and Fe^{3+} ions, possibly exhibiting charge ordering. In the low-T regime, the electrons should usually be localized in the potential wells created by the Fe ions. The average Fe−Fe distance may thus be considered as an estimate of ξ in Eq. 4. There are twelve such unique distances apparent in the structure, two for each pair of Fe−Fe bonds (1-2, 1-3, 1-4, 2-3, 2-4, and 3-4), within the kagomé layer and in between the triangular and kagomé layers, as illustrated in Fig. 4(c) for CBFO3 at 300 K. These are averaged to get ξ from which the range R is calculated, as listed in Table II. The values of R obtained indicate the short-range nature of polaron hopping conduction by VRH mechanism, similar to some examples in the literature [27, 28, 35, 36]. At this juncture, it may be noted that the dc resistivity data includes grain-boundary effects in addition to grain-intrinsic response. However, for bulk samples like ours, the derived parameters and the functional dependence do not deviate significantly from the ideal sample response. Nevertheless, the grain-intrinsic response of the dc resistivity can be extracted from ac measurements, which will be discussed in Sec. III D, in connection with the data corresponding to the filled symbols in the main panel and inset of Fig. 4(b). We will see that the results are close to that represented here.

D. AC conductivity analysis

Study of ac impedance spectroscopy is very useful in polycrystalline specimens as it is possible to isolate grain-intrinsic response from the extrinsic contributions arising from grain-boundary and electrode-contact interfaces, because the relaxation times of charge carriers are of different orders in each case. The extrinsic effects occur at lower frequencies, but are frozen at high frequencies, where the intrinsic effects are activated. The extrinsic effects can be distinguished from the intrinsic contribution in the frequency scale upon observing the evolution of the f-dependent features with temperature. Real part of the frequency dependent ac conductivity ($\sigma_{\rm tot}$) is shown in Fig. 5(a), (b), (c), and (d) at various representative temperatures. $\sigma_{\rm tot}$ is obtained directly from the raw data using $\sigma_{\rm tot} = Gd/A$, where d is the thickness of the sample and A is the area of silver plating. The $\sigma_{\rm tot}$ curves show two distinct regions separated by a step-like increase. In each such region, the low-f end is a frequency-independent plateau representing the dc contribution while the high-f end is dispersive. This kind of behavior is usually explained by Jonscher's power law [37–39]

$$\sigma_{\rm tot}(\omega) = \sigma' = \sigma_{\rm dc} + \sigma_0\omega^s, \tag{5}$$

where σ' represents real conductivity, $\sigma_{\rm dc}$ represents dc conductivity and $\sigma_0\omega^s$ ($=\sigma_{\rm ac}$) represents ac conductivity. σ_0 is a temperature-dependent pre-factor, ω is the angular frequency of the applied ac electric field signal, and s is a temperature-dependent frequency exponent. Dielectric response of diverse materials were found to obey this power law behavior and hence was termed as Universal Dielectric Response (UDR) by Jonscher [39–41]. Non-zero values of s represent dispersive conductivity (high-f region) and arises due to back and forth hopping of polarons to neighboring sites [39, 42, 43]. Within our available f-window, we could perform unambiguous fitting of $\sigma_{\rm tot}$ data (using Eq. 5) in limited T-ranges, as shown by the red curves in Fig. 5(a), (b), (c), and (d), from which we obtained the parameter 's' as a function of temperature. At lower T, the data are scattered significantly and at higher T the relevant features of the data drift out of our f-window. In the UDR model, the imaginary part of the conductivity (σ'') is given by [29, 39],

$$\sigma''(\omega) = \sigma_0\omega^s \tan(s\pi/2) + \omega\epsilon_0\epsilon_\infty, \tag{6}$$

where ϵ_0 is the static dielectric constant and ϵ_∞ is the high frequency limit of the dielectric constant. This is related to the real dielectric permittivity (ϵ') by [39],

$$\epsilon'(\omega) = \sigma''/(\omega\epsilon_0) = \epsilon_\infty + (\sigma_0/\epsilon_0)\omega^{s-1}\tan(s\pi/2). \tag{7}$$

The fitting of the high-frequency intrinsic part of the ϵ' data using Eq. 7 is shown in Fig. 5(e), (f), (g), and (h), from which we again obtained values of 's' as a function of temperature. The values of s obtained from both the fits are in good agreement with each other. s obtained from the $\sigma_{\rm tot}$ vs. f fitting are plotted with temperature in Fig. 5(i), (j), (k), and (l), the nature of which provides information about the hopping dynamics of charge. s obtained from the ϵ' vs. f fitting is included in Fig. S7 of the supplemental material [21]. The value of s decreases steadily from a high value close to unity. This kind of behavior is predicted for overlapping large polarons whose

TABLE III. Parameters obtained from ac conductivity, and electric modulus analysis.

Sample	OLPT model			Electric modulus	
	E_H (meV)	τ (s)	r_0' —	τ_{M0} (s)	E_M (meV)
CBFO	37.0(±0.5)	1.05×10^{-08}	1.31(±0.05)	3.88×10^{-12}	182.9(±3.8)
CBFO1	46.9(±0.3)	1.91×10^{-09}	3.06(±0.07)	1.64×10^{-12}	225.1(±4.0)
CBFO3	41.6(±0.6)	3.14×10^{-08}	0.93(±0.03)	1.35×10^{-13}	218.5(±2.2)
CBFO5	40.4(±0.2)	2.87×10^{-08}	1.24(±0.07)	5.76×10^{-13}	215.5(±2.5)

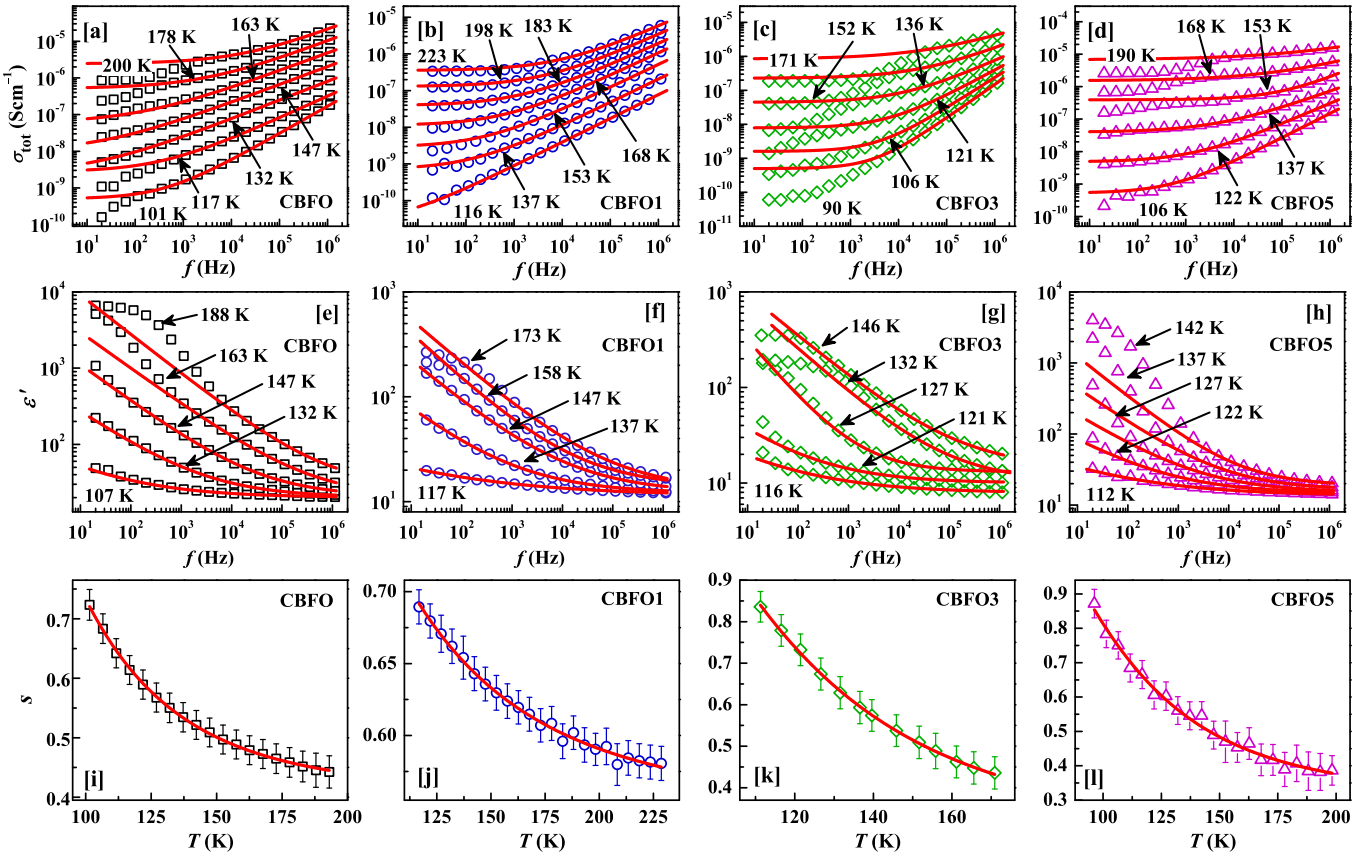

FIG. 5. (a), (b), (c), and (d): Variation of ac conductivity with frequency [$\sigma_{\rm tot}(f)$], fitted using UDR model (red curves), Eq. 5, for CBFO, CBFO1, CBFO3, and CBFO5, respectively. (e), (f), (g), and (h): Variation of real permittivity with frequency [$\epsilon'(f)$], fitted using UDR model (red curves), Eq. 7, for CBFO, CBFO1, CBFO3, and CBFO5, respectively. (i), (j), (k), and (l): Variation of frequency exponent with temperature [$s(T)$], fitted using the OLPT model (red curves), Eq. 8, for CBFO, CBFO1, CBFO3, and CBFO5, respectively.

spatial extent is larger in comparison to the interatomic spacing and there is overlapping of the polaron distortion clouds [40, 41]. The large polaronic nature usually arises due to overlapping potential wells of neighboring sites where a long-range coulomb interaction prevails [41]. In our case, a long-range coulomb interaction of course arises due to the background electric field arising from the polar nature of the samples. T-dependence of s is fitted with Overlapping Large Polaron Tunneling model (OLPT), defined by [40],

$$s = 1 - \frac{4 + 6E_H r_0'/(k_B T R'^2)}{R'[1 + E_H r_0'/(k_B T R'^2)]^2}, \tag{8}$$

along with

$$2R' = \ln\frac{1}{\omega\tau} - \frac{E_H}{k_B T} + \left[\left\{\ln\frac{1}{\omega\tau} - \frac{E_H}{k_B T}\right\}^2 + \frac{4r_0' E_H}{k_B T}\right]^{1/2}, \tag{9}$$

where E_H is the energy barrier, r_0' is the reduced polaron radius ($r_0' = 2\alpha r_0$, r_0 being the absolute polaron radius), R' is the reduced hopping distance ($R' = 2\alpha R$, R being the absolute hopping distance), α is the polarizability of a pair of sites and τ is the inverse attempt frequency. At this juncture, it will be quite relevant to compare the T-dependence of s in case of $CaBa[Co(Cr/Ni)]_4O_7$ compounds which show monotonous increase with temperature and obey small polaron tunneling model [16]. For the purpose of data fitting, we have taken a mid-range value of frequency, $f = 10$ kHz ($\omega = 2\pi f$), while E_H, τ, and r_0' are taken as fitting parameters. The best fit values of the parameters are given in Table III. The model fits well with the data, as shown in Fig. 5(i), (j), (k), and (l) by the red curves, which is indicative of the Overlapping Large Polaron Tunneling as the dominant mechanism of ac conduction. The fitting of the s vs. T data, obtained from the ϵ' vs. f analysis, with the OLPT model is given in Fig. S7 of the supplemental material along with the parameters obtained from the fitting in Table S7 [21]. However, it may be noted that this model also effectively described the small polaron dynamics in certain oxides such as $Pr_{0.5}Ca_{0.5}MnO_3$ [44] and $Pr_{0.7}Ca_{0.3}MnO_3$ [45], while Seeger *et al.* retained the 'large polaronic' description in $La_{1-x}Ca_xMnO_3$ ($0.05 \leq x \leq 0.125$) [29]. Staveren *et al.* discussed about the applicability of the OLPT model even to the small polarons. Nevertheless, the en-

TABLE IV. VRH parameters obtained from the analysis of σ_{dc}, derived from ac conductivity analysis.

Sample	$T_0^{1/4}$ ($K^{1/4}$)	E_ρ (meV)	ξ (Å)	R (Å)	T-Range (K)
CBFO	240.81(±0.1)	166−268	3.17	65−55	101−193
CBFO1	213.74(±0.1)	163−271	3.19	56−47	117−229
CBFO3	176.77(±0.1)	117−180	3.18	48−42	96−171
CBFO5	245.99(±0.1)	163−280	3.18	67−56	96−198

tirely different T-dependence of s in CBFO compounds compared to $CaBa[Co(Cr/Ni)]_4O_7$ [16] hint at the comparatively larger polarons in the current materials, and completely different carrier dynamics. E_H obtained is an order smaller compared to the activation energies obtained in dc conduction (Table II). This points out the distinctive natures of the two mechanisms of conduction, dc and ac. The ac conduction is a much shorter range tunneling compared to the dc conduction. The magnitude of τ obtained is (in general) couple of orders larger than that observed in the $CaBa[Co(Cr/Ni)]_4O_7$ compounds [16] ($\sim 10^{-12}$ s), reminding about the reduced mobility of the larger polarons in these materials. We will further find in the next section that this high value is also due to the existence of a 'cooperative'-ness in between the polarons. The σ_{dc} obtained from the ac conductivity analysis are again plotted (as $\rho(T) = 1/\sigma_{dc}$) using VRH model (Eq. 2) in Fig. 4(b) (filled symbols). The wine colored lines indicate the fits using the VRH model which appears satisfactory. The parameters obtained from the fitting is included in Table IV. It can be noted that the overall magnitude of $\rho(T)$ has decreased slightly and the slope of the curves have increased slightly, compared to the data obtained from dc analysis. This is because the magnitude of $\rho(T)$ obtained from the dc measurements has contributions from grain-boundary, in addition to grain-intrinsic response, but the $\rho(T)$ obtained from the $\sigma_{tot}(\omega)$ analysis using Eq. 5 consists only of the grain-intrinsic response. The range of activation energy obtained using Eq. 3 is represented by filled symbols in the inset of Fig. 4(b) which is a bit larger due to the increased slope of the $\rho(T)$ curves. The lower values of activation energy in the $\rho(T)$ obtained from dc analysis is because of the higher disorder (or defects) in the grain-boundary region while the intra-grain regions are devoid of such disorder.

E. Electric modulus analysis

Complex electric modulus, $M^* = M' + iM''$, is the Fourier transform of a relaxation function $\phi(t)$ [46–52],

$$M^*(\omega) = M_\infty \left[1 - \int_0^\infty \exp(-i\omega t)(-\frac{d\phi}{dt})dt\right], \quad (10)$$

where $M_\infty = 1/\epsilon_\infty$ is the high-frequency asymptotic value of the real electric modulus $M'(\omega)$. The relaxation function is called as Kohlrausch–Williams–Watts (KWW) function given by [53],

$$\phi(t) = \exp\left[-(t/\tau)^\beta\right], \quad (11)$$

which represents the time evolution of the electric field within the material, where τ is the charge carrier relaxation time, and β ($0 < \beta \leq 1$) is a stretched exponent. Analysis of electric modulus data has the advantage of suppressing the extrinsic contributions like grain-boundary and electrode-contact so that the pristine characteristics of the sample can be studied confidently [47, 48, 51, 52]. Study of electric modulus can bring out valuable information about charge carrier dynamics and relaxation. $M'(f)$, and $M''(f)$ data are shown in Fig. 6(a), and (b) for CBFO5 while the others show similar behavior. $M'(f)$ shows thermally activated steps and $M''(f)$ shows thermally activated peaks. Overall, thus the charge carrier relaxation time (τ) increases with increasing temperature due to thermal disorder.

Owing to the broadness and the skewness of the data, the M', and M'' data could be fitted with Havriliak-Negami equation for electric modulus (and not with other simpler models), given by [54],

$$M^*(\omega) = M_\infty + \frac{M_s - M_\infty}{[1 + (j\omega\tau_M)^\alpha]^\gamma}, \quad (12)$$

where $M_s = 1/\epsilon_s$ is the static or low-frequency value of $M'(\omega)$, and $\omega = 2\pi f$. The parameter α accounts for the broadness while γ accounts for the skewness of the $M^*(f)$ curves. While $\alpha < 1$ indicates disorder and distribution in τ_M, $\gamma < 1$ indicates cooperative nature of the charge carrier dynamics [30, 51]. The real and imaginary components are given by [55]

$$M' = M_\infty + (M_s - M_\infty) \times \frac{\cos(\gamma\phi)}{[1 + 2(\omega\tau_M)^\alpha \cos(\pi\alpha/2) + (\omega\tau_M)^{2\alpha}]^{\gamma/2}} \quad (13)$$

$$M'' = (M_s - M_\infty) \times \frac{\sin(\gamma\phi)}{[1 + 2(\omega\tau_M)^\alpha \cos(\pi\alpha/2) + (\omega\tau_M)^{2\alpha}]^{\gamma/2}} \quad (14)$$

with

$$\phi = \tan^{-1}\left[\frac{(\omega\tau_M)^\alpha \sin(\pi\alpha/2)}{1 + (\omega\tau_M)^\alpha \cos(\pi\alpha/2)}\right]. \quad (15)$$

Eqs. 13 − 15 fit the electric modulus data very well, as shown in Fig. 6(a), and (b) by the solid red curves. M_∞, M_s, τ_M, α, and γ are taken as fitting parameters. The obtained values of α, and γ are displayed in Fig. 6(c), and (d), respectively. The magnitude of α varies from the highest of ~ 0.9 for CBFO5 to the lowest of ~ 0.38 for CBFO1. The data strangely points out that the distribution in τ_M, indicated by the value of α, is quite high in the parent compound CBFO (α around 0.5), and increases further for a slight doping of Dy (1%) in CBFO1 (α reduces further to ~ 0.38). But then it reduces dramatically (α increases to ~ 0.75) for further doping of

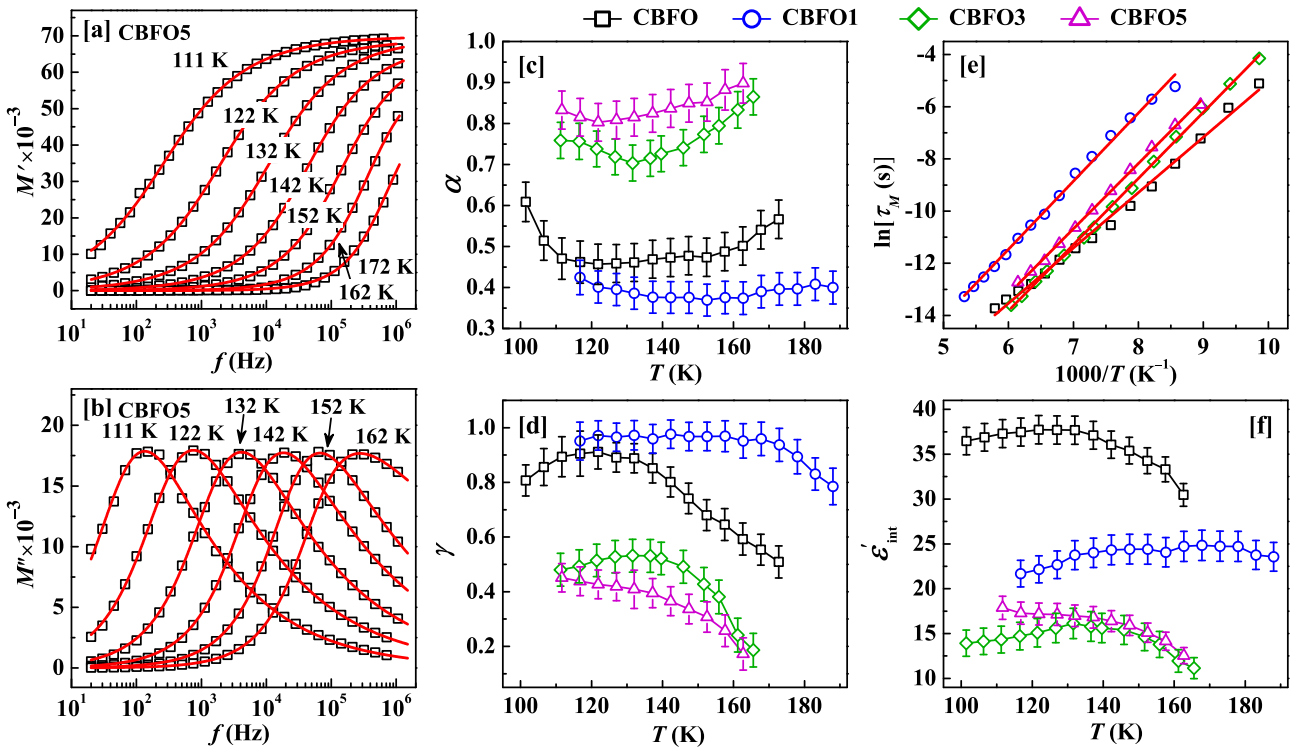

FIG. 6. Variation of the (a) real part (M'), and (b) imaginary part (M'') of electric modulus with frequency at different temperatures for CBFO5. The red curves are the fits according to the Havriliak-Negami model, Eq. 13 - 15. Temperature dependence of the parameters (c) α, and (d) γ for all the compositions. (e) Temperature dependence of the relaxation time $[\tau(T)]$ plotted and fitted using Arrhenius model, Eq. 16. (f) Temperature dependence of the grain intrinsic dielectric permittivity $[\epsilon'_{\rm int}(T)]$ for all the compositions.

Dy in CBFO3 and then in CBFO5 ($\alpha \sim 0.85$). As discussed in the next section, this variation in the nature of τ_M can be correlated to the orthorhombic distortion (D, defined in Sec. III F) induced by chemical substitution. The orthorhombic distortion is initially increased by 1%-Dy doping, but then it drastically decreases upon further doping. γ shows a similar but inverse systematic variation with composition, compared to α. γ initially increases from CBFO to CBFO1 and then gradually decreases for CBFO3, and then for CBFO5. Further, α shows an overall increasing tendency with temperature while γ shows an overall decreasing tendency.

The agreement of the ac conductivity with the OLPT model hints at the role of a long-range Coulomb interaction leading to overlapping of neighboring potential wells [41]. This is indeed satisfied by the polar lattice of the materials concerned here. Besides, the cooperativeness observed cannot be only a function of carrier density in our samples, because in that case, CBFO (with no doping) should have the highest value of γ (least cooperativeness) and it should decrease systematically with increasing electron doping via Dy substitution for Ca. But this is not the scenario here. It however seems plausible that the long-range internal electric field of the polar lattice may play a major role in driving the cooperativeness and may thus be correlated to the value of γ. Additionally, the correspondence between the variation of γ and D points out a possible correlation of the orthorhombic distortion with the pyroelectricity. It thus appears likely that pyroelectricity is weakened (γ closer to 1) with increasing distortion and strengthened (γ lesser than 1) with decreasing distortion and that larger structural disorder is detrimental to the pyroelectric nature of CBFO. However, further studies are required to confirm this.

At this point it is relevant to note that $\gamma \sim 0.95$ for $CaBaCo_4O_7$ (CBCO) [16], in the observed T-range of 70 - 130 K, while for CBFO, in the current study, γ increases initially from 0.8 at 100 K, extends up to 0.9 for a small T-range and then gradually decreases up to 0.5 at $\sim$ 175 K. Although being largely T-dependent, γ is on the average roughly $\sim$ 0.7 in CBFO in the observed T-range, quite smaller than that in CBCO. As per our interpretation, this in a way hints to larger internal electric field in CBFO than CBCO. The cooperativeness is probably also responsible for the larger value of τ (in ac conductivity) of the current samples, compared to $CaBa[Co(Cr/Ni)]_4O_7$ [16]. It may further be noted that for CBFO, γ increases with decreasing temperature, shows a maximum at $\sim$ 125 K and then decreases again, indicating that with decreasing T the polarization decreases up to 125 K and then increases again. Interestingly, the increase below 125 K (up to 80 K) is

also noted for the magnetic field induced polarization of CBFO (ΔP) at 14 T magnetic field (H) measured along the c direction with H along c [3].

The relaxation time (τ_M) in the above equations is the peak-value of the M'' curve. τ_M obtained from the fits is plotted in Fig. 6(e) and fitted using the Arrhenius formula

$$\tau_M = \tau_{M0} \exp(E_M/k_B T), \tag{16}$$

where τ_{M0} is the inverse attempt frequency, and E_M is the activation energy. The parameters obtained from the linear fitting are given in Table III. Values of E_M obtained are of similar order as obtained in dc-conductivity analysis (Table II) and are in accordance with other materials that exhibit polaron relaxation in the charge carrier dynamics [27, 29, 56–59]. An estimate of grain intrinsic dielectric permittivity ($\epsilon'_{\rm int}$) (devoid of extrinsic effects and which essentially constitutes contributions from dipoles and hopping polarization) is given by $\sim 1/(M_\infty - M_s)$, plotted in Fig. 6(f). The parent compound CBFO is found to have the highest value ~ 35. The magnitude is found to decrease considerably to ~ 24 for 1% Dy doping in CBFO1. With further increase of doping to 3 and 5%, for CBFO3 and CBFO5, respectively, the value nearly saturates to ~ 15. The data indicates that the slightest doping at the Ca-site largely disrupts the polarization in the material with the effect saturating around 5% doping. The overall low value of $\epsilon'_{\rm int}$ in spite of the existing polarization is due to the random orientations of the crystallites (in the polycrystalline specimens) which are polar along a fixed direction (here, c-direction).

F. Correlation with crystal structure

The variation of the Havriliak-Negami exponents, α, and γ, with doping percentage of Dy can be correlated with the structural parameters obtained from Rietveld refinement of x-ray diffraction patterns (Fig. 1). Fig. 7(a), (b), (c), and (d) show the variation of the lattice constants a, b, c, and the unit cell volume V with temperature for all the compositions. For CBFO, and CBFO5 the magnitudes of a, b, and V are close to each other, with differences occurring at lowest temperatures and near room temperature, while that of c is quite different. The other two compositions show considerable differences in the parameters. The orthorhombic distortion (D), defined as $D = \sqrt{2}b/(a+c)$, is plotted in Fig. 7(e) with temperature for all the compositions. D shows systematic variation with composition while exhibiting a mild overall increasing trend with temperature. This variation of D with composition has remarkable similarity with the variation of α, and γ [Fig. 6(c), and (d)] indicating the direct correlation of the distribution of τ_M, and 'cooperative'-ness of charge carrier relaxation, with structural distortion. A clear picture of the variation of D with Dy doping percentage can be seen in Fig. 7(f). Considering any one of the temperatures, say 23 K, D initially decreases from a value of 0.9350 for CBFO to a minimum value of 0.9317 for CBFO1, and then increases steadily for CBFO3 and CBFO5, until it reaches 0.9346 for CBFO5 which is very close to the value of CBFO. The behavior is similar for all the temperatures, with a slight variation in the magnitude that increases mildly with T [more obvious in Fig. 7(e)]. Similar variation of α, and $1-\gamma$ is observed in Fig. 7(g), and 7(h), respectively, replotted as a function of Dy doping percentage. A definite correlation, however, cannot be found for the temperature dependence of γ with D. This is because, firstly, γ is available in a narrow T-range in between 100 K and 190 K, limited by the frequency range of the LCR meter. Secondly, the accuracy of the obtained values of γ and D (indicated by the error bars) is not precise enough to discuss the T-dependence within the narrow T-range. However, the accuracy is enough to clearly point out the variation with doping percentage of Dy: $1-\gamma$ and D follows the same nature at all temperatures.

Further, an anomaly may be noted in the values of the ac conductivity parameters in Table III. The reduced polaron radius (r'_0) of CBFO1 is considerably larger (~ 3) than the other compositions (~ 1) while the inverse attempt frequency (τ) is one order of magnitude smaller ($\sim 10^{-10}$ s) than the rest ($\sim 10^{-9}$ s). This hints to the larger size of polarons in case of CBFO1 than the rest, but being decoupled from other polarons, possibly because of the high degree of structural distortion observed in the composition. Indeed, Fig. 6(d) shows $\gamma \sim 1$ indicating non-cooperative motion.

IV. SUMMARY AND CONCLUSIONS

We have demonstrated the drastic effects of Dy doping in the Ca site of $CaBaFe_4O_7$, even by a very small percentage ($x \leq 5\%$), in bulk polycrystalline specimens. The compounds exhibit an effective valency of $\sim Fe^{2.5+}$, pointing out a mixed valency of Fe^{2+} and Fe^{3+} in almost equal proportions. The dc resistivity analysis (ρ) shows variable range hopping of charge carriers as the leading mechanism of dc conduction in an extensive low-T range for all the specimens, indicative of polaron hopping conduction. The ac conductivity analysis ($\sigma_{\rm tot}$) obeys UDR behavior signifying a short range polaron hopping scenario for ac conduction. The T-dependence of the frequency exponent 's' obtained from the $\sigma_{\rm tot}$ analysis obeys OLPT model designating large polaronic nature of the charge carriers, also evident from the magnitude of the relaxation time (τ). The distinctive magnitude of the activation energy (E_H) compared to that obtained from dc conduction hints towards unique dynamics of the polarons in dc and ac conduction. The electric modulus analysis shows the agreement of the data with the Havriliak-Negami model which predicts the existence of a cooperative nature of dielectric relaxation in addition to the distribution in relaxation times. The distribu-

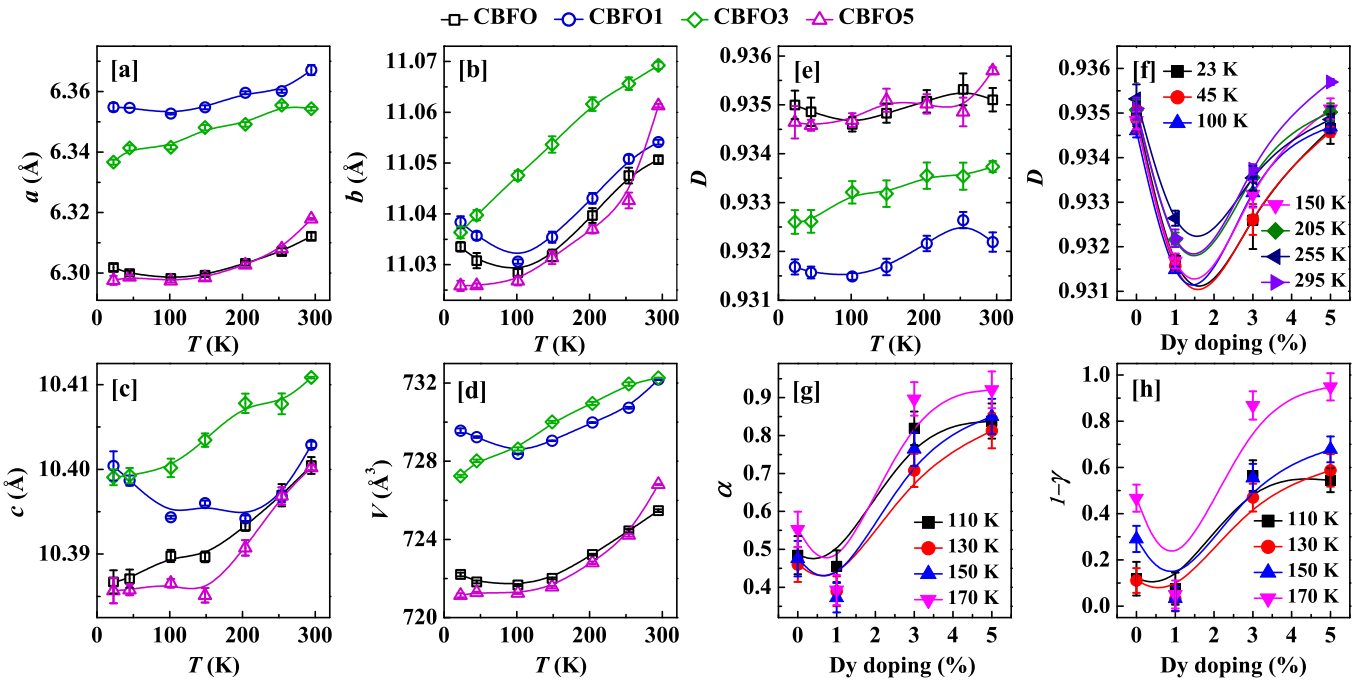

FIG. 7. (a), (b), (c), (d), (e): Temperature dependence of the lattice constants a, b, c, the unit cell volume V and the orthorhombic distortion index D, respectively, for all the compounds. Most of the error bars in these figures are within the dimensions of the data point symbols. (f), (g), (h): Dependence of D, α, and $1-\gamma$, respectively, on the Dy-doping percent of the compounds, at different temperatures.

tion parameter α and the cooperativeness parameter γ varies systematically with the Dy-doping percentage and bears close resemblance with the variation of orthorhombic distortion (D). This cooperativeness also leads to the low mobility of the polarons observed in ac conduction. The observations therefore conclude the direct correlation of the structural distortion with the charge carrier dynamics and dielectric relaxation in the materials. Apparently, the most distorted composition CBFO1 is quite interesting and we recommend further study with higher resolution synchrotron powder XRD and XAFS.

V. ACKNOWLEDGMENT

Major portion of the work was carried out using the facilities of UGC-DAE CSR. M. Islam, and A. Karmakar acknowledge the financial support from UGC-DAE-CSR through the CRS projects UGC-DAE-CSR-KC/CRS/19/MS05/0936 and CRS/2022-23/02/817. Large amount of this work was performed in the Xpress beamline, Elettra Sincrotrone Trieste. The authors sincerely appreciate the financial support granted by ICTP through the ICTP-Elettra Users Programme. Portions of this research were also carried out at the P64 beamline of the PETRA III light source of DESY, a member of the Helmholtz Association (HGF); and the financial support by the Department of Science & Technology (Government of India), provided within the framework of the India@DESY collaboration, is gratefully acknowledged. M. Islam, and A. Karmakar are grateful to Akhil Tayal for technical support during the experiments in the P64 beamline of DESY. M. Islam, S. Adhikari, and A. Karmakar greatly appreciate USIC, University of North Bengal, for SEM measurements, and GB of SSM for administrative support for executing the research works. D. De acknowledges SERB Project - EMR/2017/001195, UGC-DAE CSR Projects - CRS/2021-22/02/503 and CRS/2021-22/02/492 for financial support. D. De, and A. Karmakar are sincerely thankful to Frederico Gil Alabarse for technical support during experiments in the Xpress beamline of Elettra Sincrotrone Trieste.

[1] V. Caignaert, V. Pralong, A. Maignan, and B.Raveau, Orthorhombic kagome cobaltite $CaBaCo_4O_7$: A new ferrimagnet with a T_C of 70 K, Solid State Comm. **149**, 453 (2009).

[2] N. Hollmann, M. Valldor, H. Wu, Z. Hu, N. Qureshi, T. Willers, Y.-Y. Chin, J. C. Cezar, A. Tanaka, N. B. Brookes, and L. H. Tjeng, Orbital occupation and magnetism of tetrahedrally coordinated iron in $CaBaFe_4O_7$,

Phys. Rev. B **83**, 180405(R) (2011).
[3] V. Kocsis, Y. Tokunaga, S. Bordács, M. Kriener, A. Puri, U. Zeitler, Y. Taguchi, Y. Tokura, and I. Kézsmárki, Magnetoelectric effect and magnetic phase diagram of a polar ferrimagnet $CaBaFe_4O_7$, Phys. Rev. B **93**, 014444 (2016).
[4] G. Catalan and J. F. Scott, Physics and applications of Bismuth Ferrite, Adv. Mater. **21**, 2463 (2009).
[5] A. Huq, J. Mitchell, H. Zheng, L. Chapon, P. Radaelli, K. Knight, and P. Stephens, Structural and magnetic properties of the kagomé antiferromagnet $YbBaCo_4O_7$, J. Solid State Chem. **179**, 1136 (2006).
[6] A. Maignan, V. Caignaert, D. Pelloquin, S. Hébert, V. Pralong, J. Hejtmanek, and D. Khomskii, Spin, charge, and lattice coupling in triangular and kagomé sublattices of CoO_4 tetrahedra: $YbBaCo_4O_{7+\delta}$ ($\delta = 0$, 1), Phys. Rev. B **74**, 165110 (2006).
[7] W. Schweika, M. Valldor, and P. Lemmens, Approaching the ground state of the kagomé antiferromagnet, Phys. Rev. Lett. **98**, 067201 (2007).
[8] M. Valldor, N. Hollmann, J. Hemberger, and J. A. Mydosh, Structure and properties of the kagomé compound $YBaCo_3AlO_7$, Phys. Rev. B **78**, 024408 (2008).
[9] M. M. Seikh, T. Sarkar, V. Pralong, V. Caignaert, and B. Raveau, Dramatic effect of A-site substitution upon the structure and magnetism of the "114" $CaBaCo_4O_7$ cobaltite, Phys. Rev. B **86**, 184403 (2012).
[10] K. Dey, A. Indra, A. Chatterjee, S. Majumdar, U. Rütt, O. Gutowski, M. V. Zimmermann, and S. Giri, Chemical-pressure-driven orthorhombic distortion and significant enhancement of ferroelectric polarization in $Ca_{1-x}La_xBaCo_4O_7$ ($x \leq 0.05$), Phys. Rev. B **96**, 184428 (2017).
[11] R. D. Johnson, K. Cao, F. Giustino, and P. G. Radaelli, $CaBaCo_4O_7$: A ferrimagnetic pyroelectric, Phys. Rev. B **90**, 045129 (2014).
[12] R. S. Fishman, S. Bordács, V. Kocsis, I. Kézsmárki, J. Viirok, U. Nagel, T. Rõõm, A. Puri, U. Zeitler, Y. Tokunaga, Y. Taguchi, and Y. Tokura, Competing exchange interactions in multiferroic and ferrimagnetic $CaBaCo_4O_7$, Phys. Rev. B **95**, 024423 (2017).
[13] B. Raveau, V. Caignaert, V. Pralong, D. Pelloquin, and A. Maignan, A series of novel mixed valent ferrimagnetic oxides with a T_C up to 270 K: $Ca_{1-x}Y_xBaFe_4O_7$, Chem. Mater. **20**, 6295 (2008).
[14] K. Singh, V. Caignaert, L. C. Chapon, V. Pralong, B. Raveau, and A. Maignan, Spin-assisted ferroelectricity in ferrimagnetic $CaBaCo_4O_7$, Phys. Rev. B **86**, 024410 (2012).
[15] M. Islam, S. Adhikari, S. Pramanick, S. Chatterjee, and A. Karmakar, Remarkable effects of dopant valency - a comparative study of $CaBaCo_{3.96}Cr_{0.04}O_7$ and $CaBaCo_{3.96}Ni_{0.04}O_7$, J. Magn. Magn. Mater **529**, 167847 (2021).
[16] M. Islam, S. Adhikari, S. Das, S. Chatterjee, D. O. de Souza, G. Aquilanti, and A. Karmakar, Impurity level substitution of Cr and Ni in $CaBaCo_4O_7$ - a dielectric study, Mater. Res. Bull. **161**, 112173 (2023).
[17] C. Dhanasekhar, A. K. Das, and A. Venimadhav, Multiple caloric effects in geometrically frustrated "114" $CaBaCo_4O7$ cobaltite, J. Magn. Magn. Mater **418**, 76 (2016).
[18] J. Rodriguez-Carvajal, An introduction to the program FullProf 2000, Laboratoire Léon Brillouin (2001), homepage: https://www.ill.eu/sites/fullprof/index.html.
[19] K. Momma and F. Izumi, VESTA 3 for three-dimensional visualization of crystal, volumetric and morphology data, J. Appl. Crystallogr. **44**, 1272 (2011).
[20] W. A. Caliebe, V. Murzin, A. Kalinko, and M. Görlitz, High-flux XAFS-beamline P64 at PETRA III, AIP Conference Proceedings **2054**, 060031 (2019).
[21] Supplemental material: Rietveld refinement plots and refinement parameters of powder x-ray diffraction patterns of CBFO, CBFO1, CBFO3 and CBFO5 at all measured temperatures. UDR fits of ϵ' vs. f plots at some representative temperatures.
[22] V. Cuartero, J. Blasco, G. Subías, J. García, J. A. Rodrǵuez-Velamazán, and C. Ritter, Structural, magnetic, and electronic properties of $CaBaCo_{4-x}M_xO_7$ (M = Fe, Zn), Inorg. Chem. **57**, 3360 (2018).
[23] N. Mott and E. Davis, Electronic processes in non-crystalline materials, Clarendon, Oxford, Oxford University Press (1971), ISBN 9780199645336.
[24] N. F. Mott, Conduction in glasses containing transition metal ions, J. Non-Cryst. Solids **1**, 1 (1968).
[25] S. K. Deshpande, S. N. Achary, R. Mani, J. Gopalakrishnan, and A. K. Tyagi, Low-temperature polaronic relaxations with variable range hopping conductivity in $FeTiMO_6$ (M = Ta, Nb, Sb), Phys. Rev. B **84**, 064301 (2011).
[26] R. Kumar, S. K. Arora, I. V. Shvets, N. E. Rajeevan, P. P. Pradyumnan, and D. K. Shukla, Structural and transport properties of Bi-substituted Co_2MnO_4, J. Appl. Phys. **105**, 07D910 (2009).
[27] A. Karmakar, S. Majumdar, and S. Giri, Polaron relaxation and hopping conductivity in $LaMn_{1-x}Fe_xO_3$, Phys. Rev. B **79**, 094406 (2009).
[28] A. Karmakar, S. Majumdar, and S. Giri, Tuning A-site ionic size in $R_{0.5}Ca_{0.5}MnO_3$ (R = Pr, Nd and Sm): robust modulation in dc and ac transport behavior, J. Phys.: Condens. Matter **23**, 495902 (2011).
[29] A. Seeger, P. Lunkenheimer, J. Hemberger, A. A. Mukhin, V. Y. Ivanov, A. M. Balbashov, and A. Loidl, Charge carrier localization in $La_{1-x}Sr_xMnO_3$ investigated by ac conductivity measurements, J. Phys.: Condens. Matter **11**, 3273 (1999).
[30] P. Pal and A. Ghosh, Broadband dielectric spectroscopy of BMPTFSI ionic liquid doped solid-state polymer electrolytes: Coupled ion transport and dielectric relaxation mechanism, J. Appl. Phys. **128**, 084104 (2020).
[31] D. Liu, S. J. Clark, and J. Robertson, Oxygen vacancy levels and electron transport in Al_2O_3, Appl. Phys. Lett. **96**, 032905 (2010).
[32] C. Ang, Z. Yu, and L. E. Cross, Oxygen-vacancy-related low-frequency dielectric relaxation and electrical conduction in $Bi:SrTiO_3$, Phys. Rev. B **62**, 228 (2000).
[33] C. Ang, Z. Yu, and L. E. Cross, Oxygen-vacancy-related dielectric anomalies in $La:SrTiO_3$, Appl. Phys. Lett. **74**, 3044 (1999).
[34] A. Peláiz-Barranco, J. D. S. Guerra, R. López-Noda, and E. B. Araújo, Ionized oxygen vacancy-related electrical conductivity in $(Pb_{1-x}La_x)(Zr_{0.90}Ti_{0.10})_{1-x/4}O_3$ ceramics, J. Phys. D: Appl. Phys. **41**, 215503 (2008).
[35] H. Zheng, W. Weng, G. Han, and P. Du, Colossal permittivity and variable-range-hopping conduction of polarons in $Ni_{0.5}Zn_{0.5}Fe_2O_4$ ceramic, J. Phys. Chem. **C 117**, 12966 (2013).

[36] N. Khamaru, A. Das, D. Das, A. Karmakar, and S. Chatterjee, Effect of Cu-doping on the dielectric properties of MnV_2O_6 compound, J. Magn. Magn. Mater **512**, 167044 (2020).

[37] A. K. Jonscher, The 'universal' dielectric response, Nature (London) **267**, 673 (1977).

[38] A. K. Jonscher, Dielectric relaxation in solids, J. Phys. D: Appl. Phys. **32**, R57 (1999).

[39] A. K. Jonscher, Dielectric relaxation in solids, Chelsea Dielectric Press, London (1983), ISBN 0950871109.

[40] S. R. Elliott, A.c. conduction in amorphous chalcogenide and pnictide semiconductors, Adv. Phys. **36**, 135 (1987).

[41] A. R. Long, Frequency-dependent loss in amorphous semiconductors, Adv. Phys. **31**, 553 (1982).

[42] J. L. Izquierdo, G. B. nos, V. H. Zapata, and O. Morán, Dielectric relaxation and *ac* conduction in multiferroic $TbMnO_3$ ceramics: Impedance spectroscopy analysis, Curr. Appl. Phys. **14**, 1492 (2014).

[43] N. Ortega, A. Kumar, P. Bhattacharya, S. B. Majumder, and R. S. Katiyar, Impedance spectroscopy of multiferroic $PbZr_xTi_{1-x}O_3/CoFe_2O_4$ layered thin films, Phys. Rev. B **77**, 014111 (2008).

[44] A. Levstik, C. Filipič, V. Bobnar, D. Arčon, S. Drnovšek, J. Holc, Z. Trontelj, and Z. Jagličić, Ordering of polarons in $Pr_{0.5}Ca_{0.5}MnO_3$, Solid State Commun. **150**, 1249 (2010).

[45] A. Levstik, C. Filipič, V. Bobnar, A. Potočnik, D. Arčon, S. Drnovšek, J. Holc, and Z. Jagličić, Ordering of polarons in the charge-disordered phase of $Pr_{0.7}Ca_{0.3}MnO_3$, Phys. Rev. B **79**, 153110 (2009).

[46] I. M. Hodge, M. D. Ingram, and A. R. West, A new method for analysing the a.c. behaviour of polycrystalline solid electrolytes, J. Electroanal. Chem. Interf. Electrochem. **58**, 429 (1975).

[47] I. M. Hodge, M. D. Ingram, and A. R. West, Impedance and modulus spectroscopy of polycrystalline solid electrolytes, J. Electroanal. Chem. **74**, 125 (1976).

[48] I. M. Hodge, K. L. Ngai, and C. T. Moynihan, Comments on the electric modulus function, J. Non-Cryst. Solids **351**, 104 (2005).

[49] P. B. Macedo, C. T. Moynihan, and R. Bose, The role of ionic diffusion in polarisation in vitreous ionic conductors, J. Phys. Chem. **13**, 171 (1972).

[50] C. T. Moynihan, L. P. Boesch, and N. L. Laberge, Decay function for the electric field relaxation in vitreous ionic conductors, J. Phys. Chem. **14**, 122 (1973).

[51] A. Karmakar and A. Ghosh, Charge carrier dynamics and relaxation in (polyethylene oxide-lithium-salt)-based polymer electrolyte containing 1-butyl-1-methylpyrrolidinium bis(trifluoromethylsulfonyl)imide as ionic liquid, Phys. Rev. E **84**, 051802 (2011).

[52] E. Barsoukov and J. R. Macdonald, Impedance spectroscopy - theory, experiment and applications, Wiley-Interscience, John Wiley & Sons, Inc. (2005), ISBN 0-471-64749-7.

[53] G. Williams and D. C. Watts, Non-symmetrical dielectric relaxation behaviour arising from a simple empirical decay function, Trans. Faraday Soc. **66**, 80 (1970).

[54] S. Havriliak and S. Negami, A complex plane representation of dielectric and mechanical relaxation processes in some polymers, Polymer **8**, 161 (1967).

[55] F. Alvarez, A. Algería, and J. Colmenero, Relationship between the time-domain Kohlrausch-Williams-Watts and frequency-domain Havriliak-Negami relaxation functions, Phys. Rev. B **44**, 7306 (1991).

[56] J. L. Cohn, M. Peterca, and J. J. Neumeier, Low-temperature permittivity of insulating perovskite manganites, Phys. Rev. B **70**, 214433 (2004).

[57] A. Banerjee, S. Bhattacharya, S. Mollah, H. Sakata, H. D. Yang, and B. K. Chaudhuri, Comment on "Evidence for the immobile bipolaron formation in the paramagnetic state of the magnetoresistive manganites", Phys. Rev. B **68**, 186401 (2003).

[58] C. C. Homes, T. Vogt, S. M. Shapiro, S. Wakimoto, and A. P. Ramirez, Optical response of high-dielectric-constant perovskite-related oxide, Science **293**, 673 (2001).

[59] J. Wu, C. W. Nan, Y. Lin, and Y. Deng, Giant dielectric permittivity observed in Li and Ti doped NiO, Phys. Rev. Lett. **89**, 217601 (2002).